Draft version January 22, 2024
Typeset using LaTeX preprint style in AASTeX61

INTENSE WHISTLER-MODE WAVES AT FORESHOCK TRANSIENTS: CHARACTERISTICS AND REGIMES OF WAVE-PARTICLE RESONANT INTERACTION

Xiaofei Shi,[1] Terry Liu,[1] Anton Artemyev,[1,2] Vassilis Angelopoulos,[1] Xiao-Jia Zhang,[1,3] and Drew L. Turner[4]

[1]Department of Earth, Planetary, and Space Sciences and Institute of Geophysics and Planetary Physics, University of California, Los Angeles, CA, USA
[2]Space Research Institute of the Russian Academy of Sciences, Moscow, 117997, Russia
[3]Department of Physics, University of Texas at Dallas, Richardson, TX, USA
[4]The Johns Hopkins University Applied Physics Laboratory, Laurel, MD, USA

(Received January 22, 2024)

Submitted to ApJ

ABSTRACT

Thermalization and heating of plasma flows at shocks result in unstable charged-particle distributions which generate a wide range of electromagnetic waves. These waves, in turn, can further accelerate and scatter energetic particles. Thus, the properties of the waves and their implication for wave-particle interactions are critically important for modeling energetic particle dynamics in shock environments. Whistler-mode waves, excited by the electron heat flux or a temperature anisotropy, arise naturally near shocks and foreshock transients. As a result, they can often interact with suprathermal electrons. The low background magnetic field typical at the core of such transients and the large wave amplitudes may cause such interactions to enter the nonlinear regime. In this study, we present a statistical characterization of whistler-mode waves at foreshock transients around Earth's bow shock, as they are observed under a wide range of upstream conditions. We find that a significant portion of them are suficiently intense and coherent (narrowband) to warrant nonlinear treatment. Copious observations of background magnetic field gradients and intense whistler wave amplitudes suggest that phase trapping, a very effective mechanism for electron acceleration in inhomogeneous plasmas, may be the cause. We discuss the implications of our findings for electron acceleration in planetary and astrophysical shock environments.

Corresponding author: Xiaofei Shi
sxf1698@g.ucla.edu

1. INTRODUCTION

Collisionless shocks are ubiquitous throughout the universe. The plasma reflected by a collisionless shock can stream far away from it along the upstream magnetic field lines. When the field lines are quasi-parallel to the shock normal, a foreshock can form (e.g., Treumann 2009). This is a highly dynamic region just upstream of the shock where reflected particles excite many types of waves and transient structures. In particular observations at Earth's foreshock (Eastwood et al. 2005; Gosling et al. 1982) have revealed that the foreshock ions can interact with both the solar wind plasma and discontinuities transported by the wind. These interactions result in many types of foreshock transients, including: foreshock bubbles (FBs)(Omidi et al. 2010, 2020; Turner et al. 2020), hot flow anomalies (HFAs)(Schwartz et al. 2018; Lin 1997, 2002; Omidi & Sibeck 2007), and foreshock cavities (Turner et al. 2013; Liu et al. 2015; Schwartz et al. 1985; Zhang et al. 2022).

Shock acceleration is one of the main sources of energetic electrons in astrophysical systems but in order to operate eficiently it requires seed electrons with energies above the injection level (having Larmor radii larger than the shock transition width). However, the pre-acceleration mechanism of electrons to seed-electron energies is still an open question (e.g., Treumann 2009). Previous observations suggest that foreshock transients may be important for pre-accelerating electrons, and can therefore contribute significantly to shock acceleration (Wilson et al. 2016). They can do so, e.g., by capturing ambient foreshock electrons and further energizing them through betatron acceleration (Liu et al. 2019). As a foreshock transient boundary convects earthward (towards the bow shock), particles inside the core could gain additional energy through Fermi acceleration (Liu et al. 2017b; Turner et al. 2018; Omidi et al. 2021). In fact, a recent statistical study showed that electrons are almost always accelerated inside the core region of foreshock transients (Liu et al. 2017a). For these reasons, it is important to further explore the electron acceleration mechanisms in foreshock transients.

Around the bow shock and inside foreshock transients there are many field fluctuations and waves that could either directly accelerate electrons or modulate other acceleration processes (e.g., Fermi and betatron acceleration) (e.g., Oka et al. 2019; Lichko & Egedal 2020). One of the most effective wave modes for electron scattering and acceleration is electromagnetic whistler-mode waves (Gary 2005; Gurnett & Bhattacharjee 2005). These can be generated by a finite heat flux (Gary & Feldman 1977) or by the temperature anisotropy of electron distributions (Sagdeev & Shafranov 1961; Kennel 1966). There is good evidence that both of these types of anisotropy can arise when solar wind electrons interact with the bow shock and foreshock transients (e.g., Vasko et al. 2020; Page et al. 2021, and references therein). The importance of whistler-mode waves for electron scattering and acceleration at the bow shock has been extensively investigated and discussed (Hull et al. 2012; Oka et al. 2017, 2019; Amano et al. 2020). The role of these waves on electron energization around foreshock transients, however, remains to be fully understood. Although previous case studies have shown that whistler waves exist in foreshock transient environments (Wilson et al. 2013a) and may effectively scatter and accelerate electrons (Shi et al. 2020; Artemyev et al. 2022), their occurrence rate, spatial distribution, and wave properties (propagation, polarization, intensity) have not yet been studied comprehensively, for a range of events and plasma conditions. It is clear that a statistical study aimed at determining the properties and the potential contribution of whistler-mode waves for electron acceleration on foreshock environments is timely and important.

The desired statistical study of wave properties would ideally distinguish the dominant regime of wave-particle resonant interactions. Low amplitude, broad-band waves scatter electrons in the diffusive regime of resonant interactions (Kennel 1969; Lyons et al. 1972; Veltri & Zimbardo 1993; Amano et al. 2020), commonly observed in the solar wind (Tong et al. 2019a; Verscharen et al. 2022). Suficiently intense, narrow band (coherent) waves may resonate with electrons in the nonlinear regime of resonant interactions (Shklyar & Matsumoto 2009; Albert et al. 2013; Artemyev et al. 2018). Nonlinear resonant interactions include the phase trapping mechanism (O'Neil 1965; Nunn 1971), which is quite effective for electron acceleration in Earth's outer radiation belt (Chernikov et al. 1992; Ucer & Shapiro 2001; Kuramitsu & Krasnoselskikh 2005). Once the regime of nonlinear resonant interactions with electrons can be statistically established for the whistler-mode waves of interest at foreshock transients, then their investigation can proceed using the formalism developed (and statistical studies conducted) in a similarly inhomogeneous magnetic field environment, Earth's inner magnetosphere (Karpman et al. 1974; Inan & Bell 1977; Solovev & Shkliar 1986; Albert 1993).

We focus on whistler-mode waves observed around HFAs and FBs, the types of foreshock transients with the most significant plasma and field fluctuations. Whistler-mode waves occur regularly within and around them. Such transients occur at least ten times per day, particularly during conditions of above-average solar wind speed (Lu et al. 2022; Chu et al. 2017). Both transient types have a hot, tenuous core associated with strong plasma deflection. HFAs are surrounded by compressional boundaries on either side, while FBs have an upstream compressional boundary bounded by their own mini-shock. They have a scale of one to several Earth radii (R_E). Figure 1 (a) shows a sketch of an HFA that forms in response to an approaching solar wind discontinuity. The hot plasma generated in the core expands and the large-gyroradius hot foreshock ions at its edge form the core compressional boundaries at its two sides. Whistler-mode waves are observed in the core and compressional boundaries. The HFA moves (slides) anti-sunward along the bow shock (downward in the figure); the dashed blue line shows the spacecraft trajectory relative to the HFA.

Because foreshock transients occur frequently, at greater occurrence rates for increasing solar wind Mach number, and with intense whistler-mode waves within them, such structures are an important ingredient of shock environments at Earth and by inference in all astrophysical systems which are expected to harbor high-Mach-number, quasi-parallel shocks. The effect of foreshock transients on electron pre-acceleration, particularly the large amplitude whistlers within, has yet to be explored. This study will statistically assess the potential of whistler waves for electron acceleration and scattering in foreshock transients. Comprehensive (multi-instrument, multi-point), in-situ measurements in Earth's bow-shock allow us to examine these waves in great depth and draw conclusions for their astrophysical counterparts of similar upstream Mach number, plasma beta, and (duly normalized) spatial extent conditions.

2. DATA AND METHODOLOGY

We used data from the Magnetospheric Multiscale (MMS) mission which consists of four identical satellites in a tetrahedral configuration (Burch et al. 2016). The low frequency magnetic field is measured by the fluxgate magnetometer (FGM) (Russell et al. 2016) and the high frequency by the search coil magnetometer (SCM)(Le Contel et al. 2016) at a rate of 128 S/s and 8192 S/s, respectively, while in burst mode (as is the case here). The fast plasma investigation (FPI)(Pollock et al. 2016) instrument provides ion and electron measurements at a resolution of 150ms and 30ms, respectively (also in burst mode).

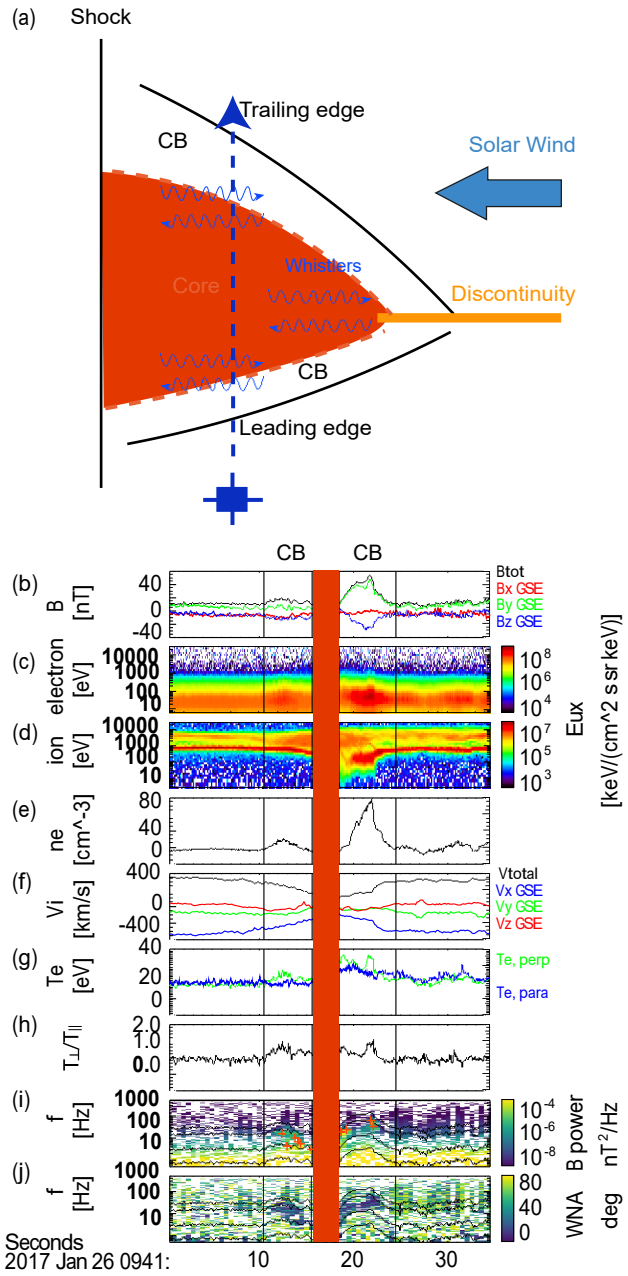

Figure 1. (a) Sketch of an HFA cross-section in the HFA reference frame, at an instant in time as it moves along the shock, past a spacecraft (down). The HFA's hot plasma core is flanked by compressional boundaries (CB). Whistler waves are observed around the edge of the core. The blue dashed line shows the spacecraft trajectory (up) relative to the HFA in this frame. (b) Magnetic field, (c,d) Energy flux of electrons and ions, (e) Electron density, (f) Plasma velocity, (g) Electron perpendicular temperature and parallel temperature, (h) Electron temperature anisotropy ($T_\perp/T_\parallel$), (i) Magnetic field power spectral density (red crosses depict mean frequency determined as discussed in the text), and (j) Wave normal angle. The core of the HFA is demarcated by the orange shaded region.

We identified 208 HFA and FB events in the MMS data collected between 2017 to 2022. They were selected using the following criteria: (1) they have a hot core with one or two compressional boundaries; (2) inside the core, density, velocity, and field strength are reduced, but temperature is increased; (3) compressional boundaries are accompanied by a sharp increase in magnetic field strength and density. Events that are overly complex and lack a clear, singular transient structure are excluded (e.g., multiple HFAs, whose boundaries are unclear). Our criteria, therefore, favor isolated events. Figure 1(b-f) represents an observation of a typical HFA with two compressional boundaries. Quasi-parallel propagating whistler waves, evidenced by an increase in wave power are observed within the compressional boundaries and on the edge of the core (Figures 1i-j). The observed whistler waves coincide with increases in the electron perpendicular temperature anisotropy (Figures 1 (g) and (h)).

We use the power spectral density (PSD) to determine the mean frequency ($\langle f \rangle$) and the frequency width (Δf) of whistler waves:

$$\langle f \rangle = \frac{\int_{f_{low}}^{f_{ce}} PSD_w \, f \, df}{\int_{f_{low}}^{f_{ce}} PSD_w \, df} \tag{1}$$

$$(\Delta f)^2 = \frac{\int_{f_{low}}^{f_{ce}} PSD_w (f - \langle f \rangle)^2 df}{\int_{f_{low}}^{f_{ce}} PSD_w df} \tag{2}$$

where $PSD_w(f) = PSD(f) - PSD_b(f)$, and $f_{low} = \max\{4Hz, f_{lh}\}$. PSD is averaged over every 0.5s and PSD_b is the background power spectrum (partly due to instrument noise), subtracted here in order to detrend the spectrograms and better reveal the waves. This background spectrum was obtained at each frequency by averaging all times when the PSD fell to < 30% of its average in each event. We used the 0.5-s (corresponding to 2 Hz) time interval for PSD, and therefore, we used 4 Hz (2 × 2Hz) as the lower frequency limit. Using the wave frequency $\langle f \rangle$ and the frequency width Δf, we compute the average wave amplitude ($\langle B_w \rangle$) and maximum wave amplitude (B_w) from band-pass filter data in each 0.5s wave interval.

Using timing and MVA (minimum variance analysis, see Sonnerup & Cahill (1968); Sonnerup & Scheible (2000)) methods to determine the magnitude and direction of the wave vector ($\vec{k}$), we then calculated the wave normal angle and the wave frequency in the plasma frame by correcting for its Doppler-shift relative to the spacecraft frame, where we measured it (note that all wave properties have been averaged at each wave measurement which is defined as the consecutive series of time points when $\int_{f_{low}}^{f_{ce}} PSD_w df > 0$). MMS provides four-point observations, from close separations. As the plasma frequency (f_{pe}) in foreshock transients is usually around 10^4Hz, the wavelength ($\lambda = 2\pi/k \sim 10s$ km, with $k = \frac{2\pi f_{pe}}{c} \sqrt{f/(f_{ce}\cos\theta_{kb} - f)} \sim f_{pe}/c$) is comparable to the average separation between the MMS satellites. Therefore, the timing method can be applied to directly obtain the value and direction of $\vec{k}$ (Paschmann & Schwartz 2000a; Turner et al. 2017). For a coherent wave signal, $\vec{k}$ obeys the following linear equations:

$$\begin{bmatrix} R_{12x} & R_{12y} & R_{12z} \\ R_{13x} & R_{13y} & R_{13z} \\ R_{14x} & R_{14y} & R_{14z} \end{bmatrix} \begin{bmatrix} k_x \\ k_y \\ k_z \end{bmatrix} = \begin{bmatrix} \Delta\varphi_{12} \\ \Delta\varphi_{13} \\ \Delta\varphi_{14} \end{bmatrix} \tag{3}$$

where R is the separation between two satellites; $\Delta\varphi = 2\pi\delta t/T$ is the phase difference between two satellites, where δt is the lag time corresponding to the peak cross-correlation and T is the observed period of the wave. The peak cross-correlations between the wave fields observed by four satellites allow us to assess the accuracy of the results. We applied the timing method at each wave measurement. For the measurements with cross-correlation > 0.8 we then calculated the mean wave frequency in the plasma frame: $2\pi f = 2\pi\langle f\rangle - \mathbf{k}\cdot\mathbf{v}_p$, where $\mathbf{v}_p$ is the plasma (ion) velocity. If the cross-correlation is smaller than 0.8, we applied an alternative method (MVA) to calculate the wave vector.

While the timing method, used above, can directly measure the magnitude and absolute direction of k, it requires coherent four-point measurements of the wave fields. For this reason, we also used the one-point MVA technique to estimate the orientation of $\mathbf{k}$ when the timing method is not applicable. The MVA method calculates the principal variance directions and their associated eigenvalues (Paschmann & Schwartz 2000a). The direction of k is the minimum variance direction. To ensure that the minimum variance direction is well determined and the waves are circularly polarized, we only kept the points with $\lambda_{int}/\lambda_{min} > 10$ (referring to the ratio of intermediate to minimum eigenvalues). We then used the wave dispersion relation to compute wave number ($|k|$) for the waves of interest(Wilson et al. 2013b). The 180° ambiguity in the k direction in the MVA method can be eliminated by using the Poynting vector S to determine the direction of k even for oblique waves (Verkhoglyadova et al. 2010, 2013) – we computed S using both electric and magnetic field data, in Appendix A from Wilson et al. (2013b), for all our events and determined the sign of wave propagation for MVA-computed k values. We then used this k to compute the Doppler-shifted wave frequency in the plasma frame from the MVA method.

3. STATISTICAL RESULTS

Whistler waves were observed in 85% of all foreshock transient events in our database. The wave spatial distribution within the foreshock transients (in the core or the compressional boundary) is important because it highlights where the waves are preferentially generated and where they may interact with electrons. To reveal the spatial distribution of whistler waves, we normalized the time interval of the core region to [0, 1], based on crossing times specific to each event. The leading and tailing boundaries were located at normalized times ≤ 0 and ≥ 1, respectively. As mentioned previously, the compressional boundary forms along the edge of the foreshock and is characterized by the enhanced magnetic field and plasma density. We defined the edge of the boundary by where the magnetic field magnitude equals the background value, where the background field was calculated by averaging the magnetic field strength in the relatively quiescent region upstream of each foreshock transient. (For example, in Figure 1 (b), the edges of the compressional boundary are shown by the vertical lines.) Note that FBs usually only have one trailing boundary. Therefore, the normalized FB event cores starting at position 0 are typically not preceded by a foreshock compressional boundary. Figures 2 and 3 depict the superposed epoch analysis of whistler wave properties and their spatial distribution in foreshock transients versus the normalized time (to be interpreted as the spatial location within the core, or relative distance from the core boundaries).

Figures 2(a,b) show the number histograms of the normalized mean frequency ($\langle f\rangle/f_{ce}$) in the core and in the compressional boundary regions of our events, respectively. The median frequency in both regions is around $0.2f_{ce}$. The spatial distribution (versus normalized time) of $\langle f\rangle/f_{ce}$ is shown in Figure 2(c). The solid and dashed black lines are the mean and median values of $\langle f\rangle/f_{ce}$; they are

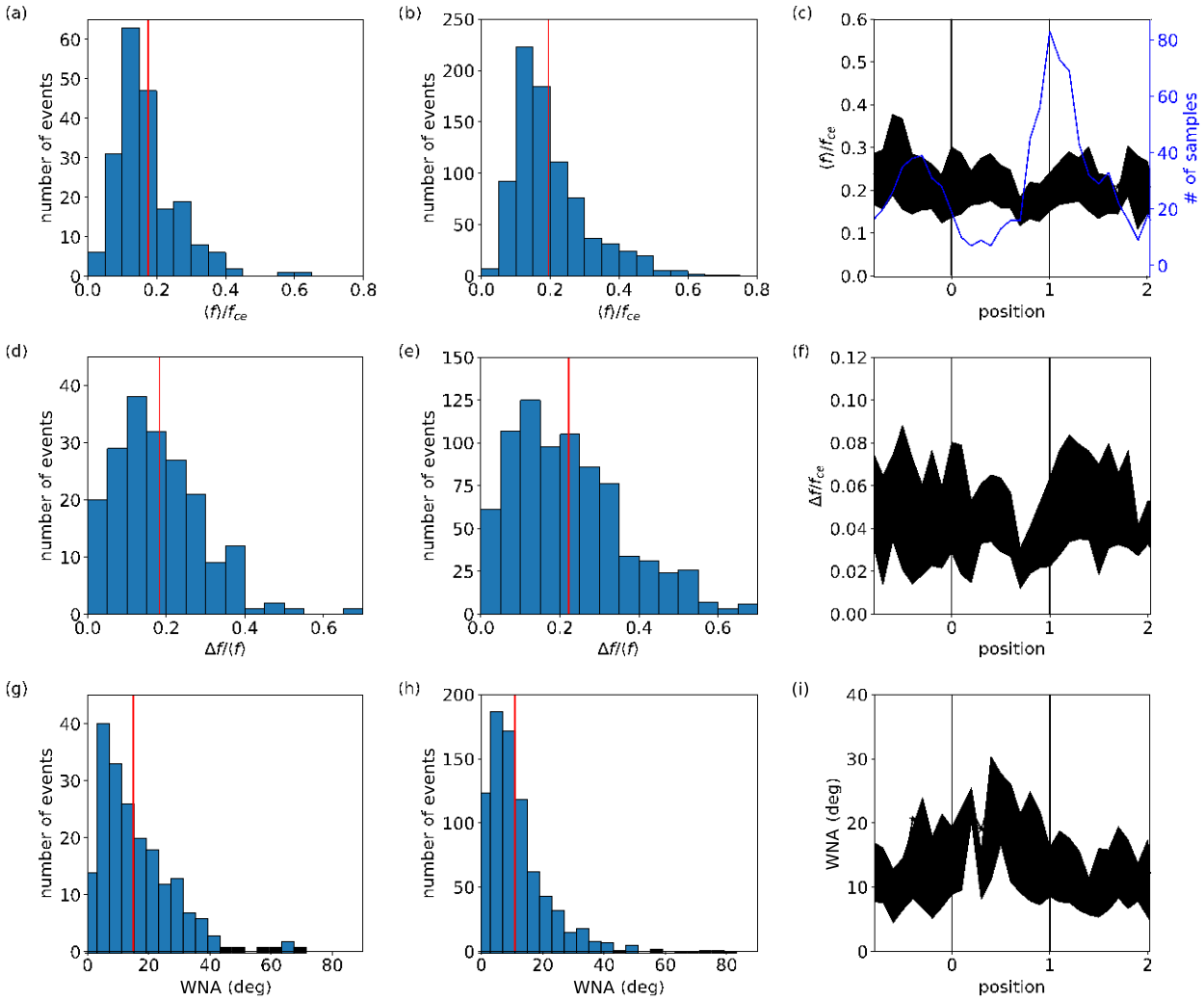

Figure 2. The number histograms and spatial distribution of: (a-c) wave frequency; (d-f) wave frequency width normalized to mean frequency; and (g-i) wave normal angle. The left and middle columns show histograms in the core and in the compressional boundaries, respectively. Dashed red lines are medians. The right column shows average and median values, in solid black lines and dashed black lines, respectively; the lower and upper bound of the shaded region represents the 25th and 75th percentile of the data, respectively; the dashed blue line in Panel (c) is the number of whistler waves observed at different locations.

191 ⍰ 0.2f_{ce} at all locations, despite the sharp change of the background magnetic field strength and 192 density at the compressional boundary. This indicates a local generation mechanism for most of the 193 observed waves.

194 There are more waves with $\langle f \rangle/f_{ce} \geq 0.3$ observed in the core, than in the boundary 195 (compare Figures 2(a) and (b)). Although this difference between the core and boundary 196 $\langle f \rangle/f_{ce}$ distribution is not large (less than 15% of total number of observations), it may 197 imply that some fraction of the waves observed in the core, especially with $\langle f \rangle/f_{ce}$ ⍰ 198 [0.3, 0.5], may be generated within the boundaries and then propagate to the core region.

Because the core region is characterized by smaller background magnetic fields, when whistler waves propagate into it, their relative frequency ($\langle f \rangle / f_{ce}$) increases.

The dashed blue line in Figure 2(c) shows the number of events with whistler waves as a function of position. It is equivalent to the spatial statistical distribution of the waves as a function of location within the foreshock transient. It shows that whistler-mode waves are most probable near the edge of the core where the magnetic field gradient is large. More events are located near position=1 versus position=0 mainly due to the following reason: the trailing boundary (at $\geq$ 1 region) is usually stronger (with higher magnetic field strength) than the leading one for foreshock transients. This feature has been shown in previous observations and simulation studies (Liu et al. (2016); Vu et al. (2022)), and Figure 1 is also an example. As a result, the change of the magnetic field strength is sharp at the region around 1 but smoother around 0. The wave generation is favorable in the region with a large field gradient where magnetic field compression drives the transverse electron heating required for wave generation, and therefore, more likely to be observed around position $\sim$1.

Figures 2 (d-f) show the number histograms and spatial distribution of the normalized wave frequency width ($\Delta f / \langle f \rangle$) in a similar manner as the frequency panels, Panels (a-c) above. The median value of $\Delta f / \langle f \rangle$ is $\sim$ 0.2 in the core and in the compressional boundaries. A large portion of the observed waves are quite narrow-banded, which suggests a narrow resonant energy range of electrons responsible for wave generation, i.e. the anisotropic electron population is bounded below and above in energy by isotropic cold and hot electrons, respectively (e.g., Fu et al. 2014; Page et al. 2021; Frantsuzov et al. 2022).

The number histograms and the spatial distribution of wave normal angles are shown in Figures 2(g-i) in a similar format as the panels above. Most whistler waves are quasi-parallel propagating, and the waves tend to be more oblique in the core region: the medians increase from 12° in the boundary to 16° in the core (Panels (h) and (g)), and this is also evident in the spatial profile of both the medians and means in Panel (i). This is likely a result of (1) wave propagation to the core region from the boundaries (whistler wave propagation in inhomogeneous magnetic field and plasma results in a wave normal angle increase, see Shklyar et al. (2004); Chen et al. (2013); Gu et al. (2021)) or (2) oblique wave generation within the core by either cyclotron or Landau resonance thanks to the suppression of Landau damping by the large parallel temperature often observed in that region (see discussion of such oblique wave generation by, e.g., Li et al. (2016)).

Number histograms and spatial distribution of the normalized maximum wave amplitude (B_w/B_0) in our events are shown in Figures 3(a-c), in a format similar to Figure 2. Here, B_0 is the background magnetic field strength - typically $\sim$ 5 – 10s nT in HFAs and FBs. The median value for B_w/B_0 in both core and compressional boundaries is larger than 0.01. Thus, the maximum wave amplitude can reach 10s – 100s of pT. The mean wave amplitude (not shown here) is about 3 times smaller than the maximum value in statistics. Figures 3 (d-f) show the distribution of electron minimum resonance energies (E_R) for the mean wave frequencies (we used equation (B1) from Wilson et al. (2013b) to calculate the resonance energy). Whistler waves are mainly resonant with electrons which have 10s – 100s of eV parallel energy. This is the hot solar wind electron halo population, having energies larger than the typical solar wind temperature.

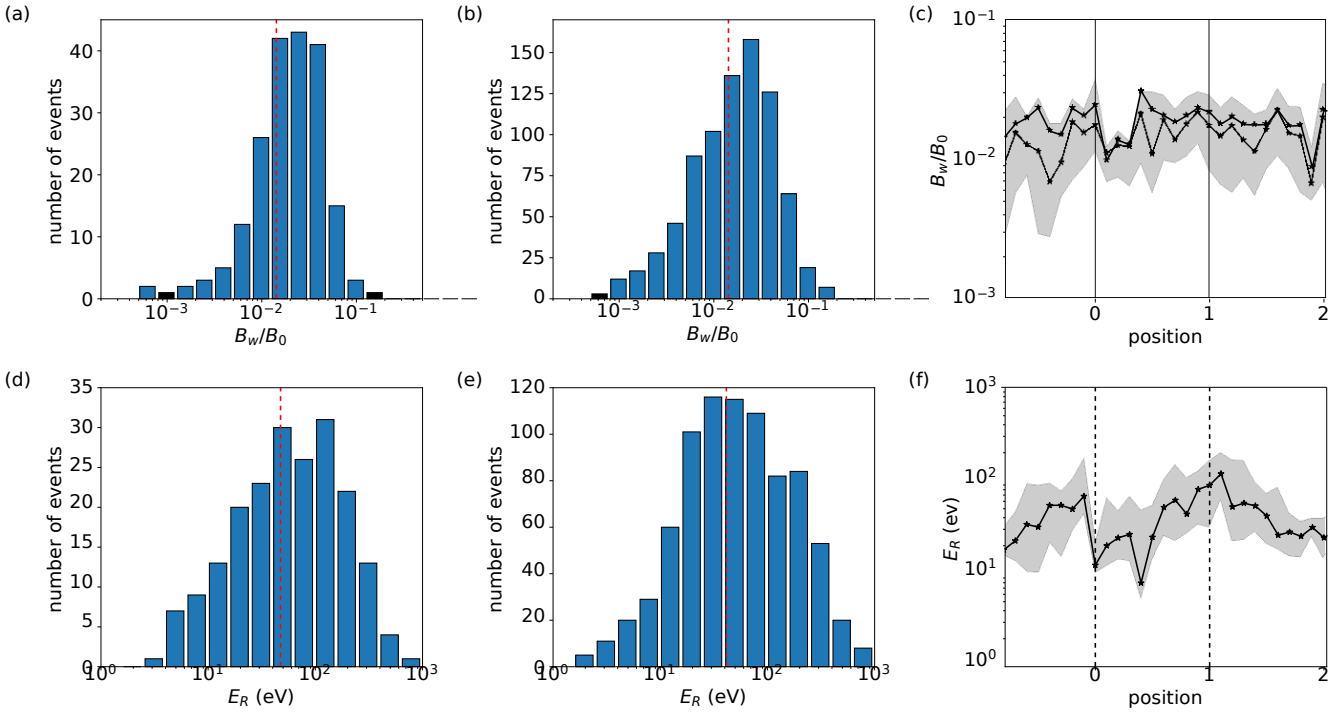

Figure 3. Number histograms and spatial distribution of (a-c) maximum wave amplitude, and (g-i) minimum resonance energy for the mean wave frequency. Dashed red lines show the median value.

The electron resonant interaction with whistler-mode waves is controlled by the wave amplitude, wave spectral width Δf, and background field inhomogeneity $\partial B_0/\partial s$. Note that s is the distance along the field, starting from the equator (in our context the latter denotes the location of minimum field magnitude). The same quantity is also used to denote the location of the interaction along the field-line direction. If the wave amplitude is low the waves cannot alter the electron orbit significantly during a single resonant interaction and the interaction remains first-order (linear) and can be described well by zero-order orbit perturbation theory (quasi-linear diffusion is a particular version of this theory see Kennel & Engelmann 1966); If the wave spectral width is too broad relative to the resonance width, nonlinearity from that resonance can also be evaded. These two conditions can be expressed as two criteria for nonlinear interaction. The first assesses the nonlinearity for a pure mode using the inhomogeneity parameter, S, a function of the normalized wave amplitude B_w/B_0 and $\partial B_0/\partial s$. The second criterion on the spectral width Δf addresses the spectral purity (the monochromatic nature) of the wave.

For highly coherent (approximately monochromatic, or pure mode) waves in an inhomogeneous magnetic field, the nonlinearity criterion for $S \approx (\partial B_0/\partial s)/(B_w/B_0)$ (Omura et al. 2008) is:

$$S = \frac{1}{2}\frac{N^2}{N^2-1}\left|\frac{kv_\perp}{f_{ce}} - 3 - \frac{N^2}{v_\perp}\cdot v_R\cdot\frac{\partial^2 B_0}{\partial s^2}\cdot\frac{1}{B_w}\frac{\partial B_0}{\partial s}\right| \qquad (4)$$

with k being the value of wave vector, $N = kc/\omega$ the wave refractive index, $v_\perp = \sqrt{v_x^2 + v_y^2}$ the electron transverse velocity, $v_R = 2\pi(f - f_{ce})/k$ the resonant velocity in km/s (k in this equation is in rads/km), and $\partial/\partial s$ the gradient along magnetic field lines. The inhomogeneity of the background

magnetic field ($\partial B/\partial s$) is computed using the linear estimation of the gradient method from four-satellite observations (see Chapter 14 of Paschmann & Schwartz (2000b)). When $|S| < 1$ the wave is suficiently strong to locally overcome the mirror force $\propto \partial B_0/\partial s$ and alter the electron trajectory significantly. This is the regime of nonlinear resonant interactions. S depends on the electron energy and pitch angle (linked by the resonance condition). For $\partial B_0/\partial s = 0$, S is finite and can be evaluated in two limits: (1) in the local limit, S_{local} evaluated explicitly shows if electrons with a given energy and pitch angle will interact with waves nonlinearly, and (2) in the global limit, S_{global} can be evaluated by projecting the electron pitch angle (α) from the location s of the wave measurements to the location where B_0 reaches its minimum. In the global limit, S_{global} captures how often along their zero-order, adiabatic trajectory ($\sin^2\alpha/B_0 = $ const) electrons will interact with the waves nonlinearly.

For each wave event in our database, we obtained the 0.5-second averaged value of the wave properties (k, $\langle\delta f\rangle$, B_w), electron cyclotron frequency f_{ce}, background field B_0, background inhomogeneity $\partial B/\partial s$, and electron parallel resonant velocity v_R. To compute S, we also need $v_\perp$ ($v \sin\alpha$) which is a function of the (total) resonance energy ($E = 1/2 m_e v^2$) and pitch angle α. (Note that the total energy and α are connected by $\cos\alpha = v_R/v$). We used this to compute S in the local limit, and from it S in the global limit.

We computed S_{local} at different energies using the (local) measurements. Combining all the local measurements, we can arrive at the number distribution and the value of S_{local} versus energy and pitch angle in our dataset. Figure 4(a) shows the distribution of the number of measurements used for this computation. The black contour shows the number of samples per bin below which lie just 5% of all observations. The region outside this contour denotes the parameter space where the number density is rather low (interpreted as insignificant) compared to the rest of the parameter space, inside that contour. Figure 4(c) shows the fraction of measurements with $|S_{local}| < 1$; it represents the probability distribution for electrons to interact with waves nonlinearly in the local limit. The 5% contour of the number of measurements is transferred here from the counts per bin panel above it. It demarcates the region within which the probability distribution is trustworthy. We see that in the region of $\alpha > 45^\circ$ and E in [300, 1000] eV the fractions are high: They are > 30% and can get up to $\propto$ 60%. In this region of (E,α) space where a suficient number of measurements exists, there is a large enough probability for $|S_{local}|$ to be < 1 (for the observed waves to be suficiently intense) such that the waves interact with electrons nonlinearly.

The global limit is obtained under the assumption that electrons are bouncing within a local magnetic field trap. In each event, we projected the local electron pitch angle to the location where B_0 reaches its minimum (around the center of the core region), and then obtained S_{global} by mapping S_{local} to a new pitch angle corresponding to that minimum. Such mapping also removes the direct connection between the electron energy and (mapped) pitch-angle through the resonant condition. The number of measurements in energy versus mapped pitch-angle space is shown in Figure 4(b) in a format similar to that of Figure 4(a), including the contours. The resultant fraction of $|S_{global}| < 1$ is shown in Figure 4(d), with contours transferred from the panel above it. It shows that $\alpha < 45^\circ$, and > 100 eV electrons will be resonant with whistle-mode waves nonlinearly (note measurements outside of 25% contour are considered not statistically representative).

Overall, Figures 4(c,d) demonstrate that in the foreshock transients of our database, quite often the whistler waves are strong enough to cause nonlinear resonant interaction with electrons; the background magnetic field inhomogeneity is too weak to suppress this nonlinear behavior. However,

the wave spectral width Δf also influences the resonant interactions. The above considerations assume that the waves are suficiently monochromatic, i.e., Δf is small enough. The criterion for small Δf can be derived from (Karpman 1974; Le Queau & Roux 1987):

$$\frac{\Delta f}{\langle f \rangle} < \frac{B_w}{B_0}\frac{v f_{pe}}{c f_{ce}}^{1/2}\frac{f/f_{ce}}{1-f/f_{ce}}^{1/4} \quad (5)$$

where v is electron velocity determined by the resonance condition ($v = v_R/\cos\alpha$). If this criterion is not satisfied, the wave spectrum is broadband (random phase approximation is valid) to break nonlinear resonance effects. If the criterion is satisfied, the phase of waves in the wave packet can be coherent and prevent random phase mixing. Similar to the S_{local} treatment, we statistically collected the distribution of RHS/LHS versus energy and pitch angles for each local measurement, where RHS and LHS are the right-hand side and left-hand side terms of Eq.(5). Then we rearranged the data to get the distribution of the wave measurements versus ($|S_{local}|$, RHS/LHS) (shown in Figure 4(e)). The region $|S_{local}| < 1$ and $RHS/LHS > 1$ corresponds to that of nonlinear resonant interactions. The requirement of a narrow wave spectrum halves the number of observed waves resonating with electrons nonlinearly, i.e., ≈ 30% of observed waves have $|S_{local}| < 1$, but only half of these waves have $RHS/LHS > 1$. But even ≈ 15% of waves populating $|S_{local}| < 1$ and $RHS/LHS > 1$ region provides a suficiently large occurrence rate of nonlinear wave-particle interactions. This occurrence rate is comparable to (or even larger than) that of electron nonlinear resonance with whistler-mode waves in the Earth's radiation belts (Zhang et al. 2019) and is much larger than the occurrence rate of electron nonlinear resonance with whistler-mode waves in the solar wind (Tong et al. 2019a).

To identify the possible source of such intense whistler-mode waves resonating with electrons nonlinearly, we examined the electron distribution function (DF) anisotropy by evaluating the transverse-to-parallel phase space density ratio, otherwise referred to as the transverse anisotropy: $DF_{\perp}/DF_{\parallel}$ (here $DF_{\perp}$ is the electron phase space density averaged over the pitch-angle range $\in [80^\circ, 100^\circ]$, whereas $DF_{\parallel}$ is the electron phase space density averaged over the pitch-angle range $\in [0^\circ, 10^\circ]$ and $\in [170^\circ, 180^\circ]$; both $DF_{\perp}$ and $DF_{\parallel}$ are evaluated in the spacecraft reference frame and thus low-energy part of these distributions can be affected by the solar wind speed). For each local measurement, we computed this quantity at all different energies. We also computed the measurement's S_{local} value assuming a fixed, representative value for $\alpha = 50^\circ$ (corresponding to a significant fraction of waves with $|S_{local}| < 1$, based on Figure 4(c)). Figure 4(f) shows the median of the aforementioned electron transverse anisotropy as a function of normalized energy E/E_R and $|S_{local}|$ value. Near the resonance energy, $E/E_R \in [0.1, 10]$, the electron anisotropy for intense waves (those with $|S_{local}| < 1$) maximizes and reaches ≈ 2. Such a high electron anisotropy should result in large whistler-mode wave growth rates and large wave amplitudes. Note a finite electron heat flux (one of the important free energy sources for whistler-mode waves via the heat flux instability (e.g., Gary & Feldman 1977; Tong et al. 2019b)) would correspond to $DF_{\perp}/DF_{\parallel} < 1$, and thus $DF_{\perp}/DF_{\parallel} > 1$ should be attributed to the transverse anisotropy of electron temperature. Such anisotropy is the free energy source for wave generation that can be further enhanced by the presence of heat flux (Vasko et al. 2020). Thus, Figure 4(f) shows that intense whistler-mode waves amplified (or directly driven) by a large electron transverse anisotropy (up to 2) may resonate with electrons nonlinearly ($|S_{local}| < 1$). However, it is noteworthy that some of the large transverse anisotropies observed at high energies ($E/E_R \in 10$) may also be generated by electron nonlinear resonant acceleration by whistler-mode waves.

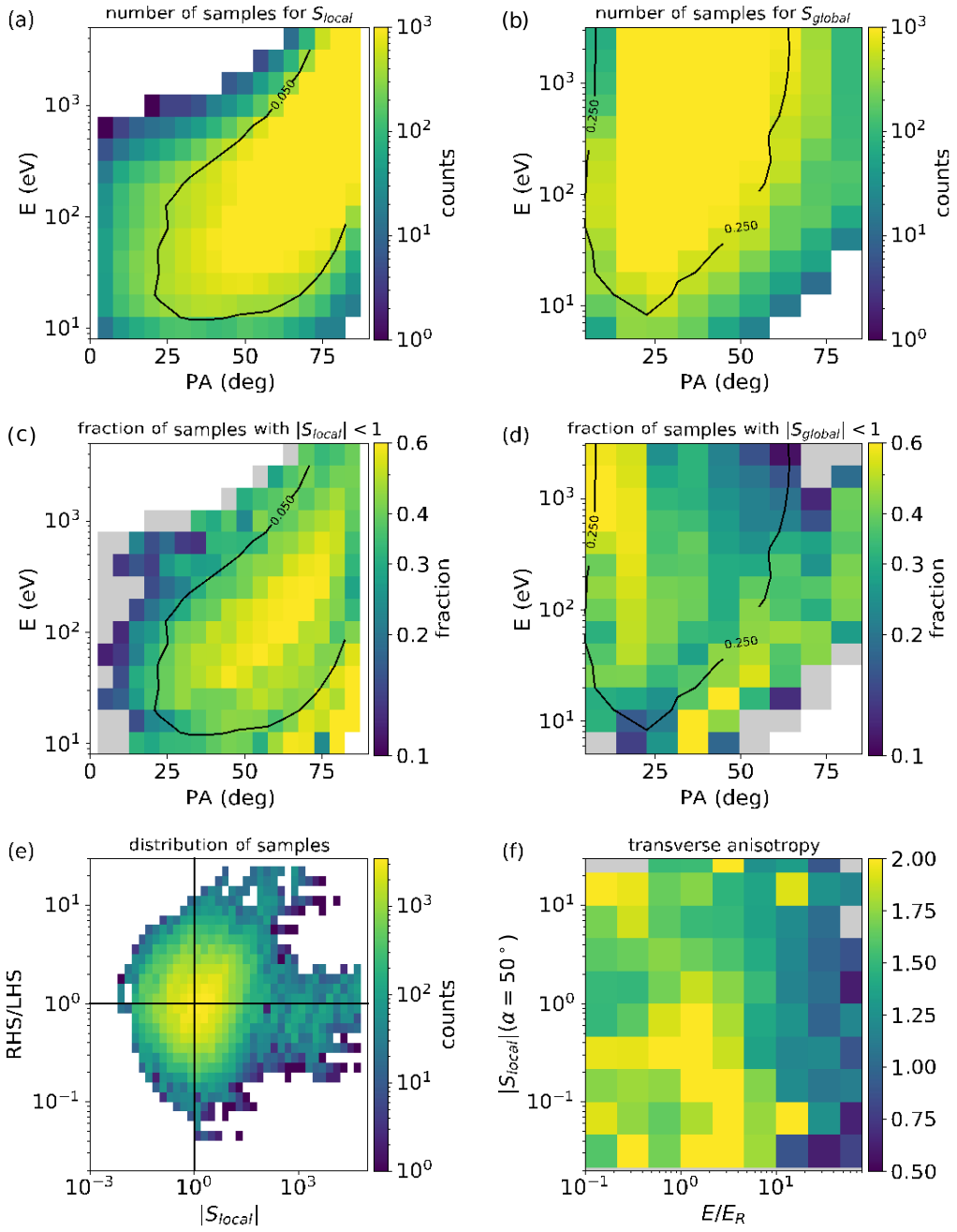

Figure 4. Panel (a, b) shows the distribution of samples for S_{local} and S_{global} calculation, respectively. The black contour shows the 95% of total samples. Panel (c) shows the sample fraction of whistler waves resonating with electrons in the nonlinear regime ($|S_{local}| < 1$). Panel (d) repeats panel (c), but for the measurements with pitch-angle adiabatically projected to the minimum of the background magnetic field from the wave observation location (S_{global}). Panel (e) shows the number of wave observations versus ($|S_{local}|$, RHS/LHS), where RHS and LHS refer to the right-hand side and left-hand side of Eq (5), respectively. $|S_{local}| < 1$ and $RHS/LHS > 1$ define the region of nonlinear wave-particle interactions (see text for details). Panel (f) shows the distribution of electron flux anisotropy versus $|S_{local}|$ and energy. Energy is normalized to the resonance energy for the observed waves.

With such a significant population of whistler-mode waves resonating nonlinearly with electrons, we anticipate the electron distributions to exhibit signatures of these interactions. Motivated by the discussion above, we separated the linear and nonlinear wave-particle interactions as follows: (1) linear regime with $|S_{local}| > 1$ or $RHS/LHS < 1$, and (2) nonlinear regime with $|S_{local}| < 1$ and $RHS/LHS > 1$.

For each wave measurement, we obtained the concurrently measured electron distribution function $DF(E, \alpha)$. We separated these DF measurements into three categories according to the wave properties: DFs associated with linear (DF_L) wave particle interactions, DFs associated with nonlinear (DF_{NL}) interactions, and no-wave DFs (DF_{NW}), those without significant whistler-mode waves observed. All electron distribution functions were normalized to the local plasma density to suppress any effects related to the strong density variations across the foreshock transients. In each transient event, we first calculated the median values of DF_{NL}, DF_L, and DF_{NW}, and their ratios (DF_L/DF_{NW} and DF_{NL}/DF_{NW}). Then we calculated the median values of these ratios. The results are shown in Figure 5(a,b); they are plotted against energy (normalized to E_R) and pitch angle. There is a clear phase space density increase around and above the resonance energy and $\alpha \approx 90^\circ$ for DF_L. This increase may be due to a combination of an initial electron anisotropy driving whistler-mode wave generation and electron acceleration by waves. A similar increase in phase space density is also evident for DF_{NL}, except it is much more localized in energy (around E_R) and covers a wider α range for DF_{NL}. If the strong DF_{NL} peak around $\alpha \approx 90^\circ$ is due to the strong initial anisotropy needed for intense wave generation, the DF_{NL} increase at small pitch-angles ($\alpha < 45^\circ$ and $\alpha > 135^\circ$) is most likely due to the effective electron mixing by nonlinear resonances with waves (see discussion of nonlinear resonant effects in, e.g., Vainchtein et al. 2018). A weak decrease of DF_L/DF_{NW} and DF_{NL}/DF_{NW} at energies well below the resonance energy is unlikely to be related to wave-particle resonant interactions but could be due to preferential wave generation within hot plasma regions where the cold electron density is reduced. The black lines in Figure 5(a,b) show the contours of DF_{NW}. Results with $DF_{NW} < 10^{-5}$ are not statistically significant because such a small phase space density may lead to large errors.

To further investigate the difference between the distributions of phase space density associated with weak and intense waves, we plot the probability distributions of $DF_L/DF_{NW} > n$ (for weak waves) and $DF_{NL}/DF_{NW} > n$ (for intense waves) over all pitch angles, where n stands for the value of the ratio. Figures 5(c,d) show the percentage of events with $DF_L/DF_{NW} > n$ and $DF_{NL}/DF_{NW} > n$ at different energies, respectively. There is a clear difference between weak and intense waves. For $DF_L/DF_{NW} > n$ around the resonance energy ($E/E_R \approx 1$) the probability distribution is reduced significantly for $n > 2$, i.e. there is nearly negligible probability of observing a phase space density increase by a factor of > 2 in association with weak waves. Conversely, for $DF_{NL}/DF_{NW} > n$ around the resonance energy the probability distribution remains large even for $n \approx 3$, i.e., there is a significant probability of observing intense waves in association with resonant phase space density increase by a factor of ≈ 3. Moreover, Figure 5(d) shows that the probability distribution has a local maximum around the resonance energy. These results are consistent with our assertion that nonlinear resonant interactions contribute significantly to electron acceleration.

4. SUMMARY AND DISCUSSION

We statistically studied whistler wave properties in foreshock transients, using a database of 208 transient events comprised of HFAs or FBs. We also investigated the regimes of wave particle

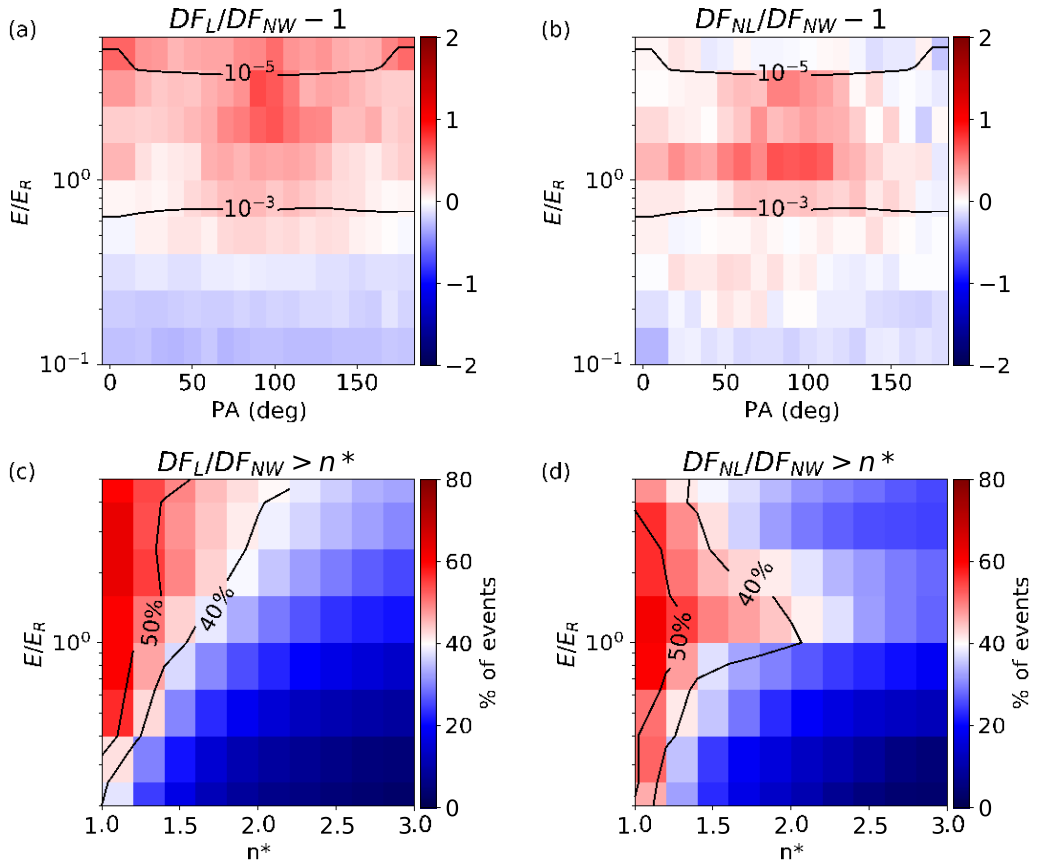

Figure 5. Electron distribution functions (DFs) collected during times when waves were observed, normalized to those collected in the absence of waves. Panels (a) and (b) show electron DFs associated with weak (a) and intense (b) wave observations normalized to the background (measured in absence of waves; subindex NW) electron spectra. Panels (c) and (d) show the probability distributions of $DF_L/DF_{NW} > n$ and $DF_L/DF_{NW} > n$, respectively. Weak waves correspond to $|S_{local}| > 1$ or RHS/LHS < 1 and are marked by subindex L, whereas intense waves correspond to $|S_{local}| < 1$ and RHS/LHS > 1 and are marked by subindex NL.

interactions and the effects of nonlinear interactions on electron distributions. Specifically, we showed that:

1. Whistler waves exist in 85% of the foreshock transients examined. These waves are most often seen around the edge of the core or the compressional boundary regions of foreshock transients.

2. The whistler waves in foreshock transients have frequencies around $0.2f_{ce}$, regardless of the abrupt change of the background magnetic field at their location. This indicates that they are generated locally, i.e., they do not propagate to the satellite from a distinctly different location in the transient or its vicinity. On average, the whistler waves are quasi-parallel. However, the waves in the core region tend to be more oblique than the waves in the compressional boundary.

3. Intense whistler waves are frequently observed. Their median amplitude is around $0.01B_0$ (10s − 100s pT). The resonance energy for electrons is around 10s − 100s eV, and 15% of

the observed whistler waves are suficiently intense and narrow-band to resonate with electrons nonlinearly.

4. Events with potential nonlinear wave-particle interactions show a clear increase in phase space density around the resonance energy. This increase is larger than that for observations associated with low-intensity waves. This suggests that nonlinear resonant interactions can contribute significantly to electron acceleration.

Recent observations of energetic electrons in foreshock transients (e.g., Wilson et al. 2016; Liu et al. 2017a) are highly suggestive that such transients can accelerate electrons and may provide a seed population for further acceleration at the bow shock - the main source of energetic particles at the dayside. Foreshock transients also exist at other high Mach number quasi-parallel shocks (e.g., at outer planets, where the solar wind Mach number is high, or occasionally even at Mars, Collinson et al. (2015)). The whistler waves studied are therefore, by analogy, likely common and significant for electron acceleration inside foreshock transients in planets and in other astrophysical contexts (such as at supernova shocks which can produce cosmic rays). Our statistical results on the whistler-mode wave intensity demonstrate that a significant portion of the observed waves resonates with electrons nonlinearly. The nonlinear interactions can play an important role in electron acceleration processes in the following way:

First, nonlinear interactions have diffusion rates that are different from (often faster than) those found in classical, linear theory. We have shown that intense waves can significantly modify electron distributions, which indicates that they can alter electron trajectories. This invalidates the approximation of unperturbed trajectories for classical scaling of electron pitch-angle diffusion rates D $\propto \langle B_w \rangle 2$ (Kennel & Engelmann 1966), and therefore, classical pitch-angle diffusion theory does not apply in such cases. If the waves propagate in short wave packets (containing only a few wave periods each; see, e.g., such wave packets in the bow shock in Hull et al. (2012); Oka et al. (2017, 2019)), then the main nonlinear effect will be the change of the diffusion rate scaling, D $\propto \langle B_w \rangle 1/2$ (e.g., Artemyev et al. 2021). In that case, a simple extrapolation of quasi-linear theory scaling, D $\propto \langle B_w \rangle 2$, to high-intensity waves would significantly overestimate the actual diffusion rate. The diffusion rate is an important element of the stochastic shock drift acceleration model (Amano et al. 2020), and therefore the change in the scaling of D may modify the eficiency of the resultant electron acceleration in this model.

Second, intense waves propagating in long wave packets (each containing tens of wave periods) may result in nonlinear resonant acceleration of electrons in an inhomogeneous magnetic field via phase trapping (see reviews by Shklyar & Matsumoto 2009; Albert et al. 2013). To be effective, this acceleration mechanism should be combined with electron periodic motions in magnetic field traps, i.e., electrons should experience multiple resonant interactions. The general magnetic field configuration of foreshock transients does allow such trapping (Liu et al. 2019). Howover, such trapping can be provided by ultra-low-frequency compressional magnetic field fluctuations (e.g., Oka et al. 2019; Lichko & Egedal 2020) and by the transient-bow shock magnetic field configuration (Liu et al. 2017b; Turner et al. 2018). Therefore, foreshock transients embedding intense whistler-mode waves (resonating with electrons nonlinearly) may serve as effective electron accelerators, if the interplanetary magnetic field can trap electrons. Further theoretical analysis of nonlinear wave-particle resonances and observational analysis of energetic electron bursts and whistler waves associated with foreshock transients may reveal the eficiency of such nonlinear resonant acceleration.

ACKNOWLEDGEMENTS

A.A. acknowledges the NASA projects 80NSSC21K0581, 80NSSC22K1634. X.-F. S. and T. Z. L. acknowledge NSF award AGS-1941012. MMS data were downloaded from https://lasp.colorado.edu/mms/sdc/pu Data access and processing was done using SPEDAS V4.1, see Angelopoulos et al. (2019).

REFERENCES

Albert, J. M. 1993, Physics of Fluids B, 5, 2744, doi: 10.1063/1.860715

Albert, J. M., Tao, X., & Bortnik, J. 2013, in Dynamics of the Earth's Radiation Belts and Inner Magnetosphere, ed. D. Summers, I. U. Mann, D. N. Baker, & M. Schulz, American Geophysical Union, doi: 10.1029/2012GM001324

Amano, T., Katou, T., Kitamura, N., et al. 2020, PhRvL, 124, 065101, doi: 10.1103/PhysRevLett.124.065101

Angelopoulos, V., Cruce, P., Drozdov, A., et al. 2019, SSRv, 215, 9, doi: 10.1007/s11214-018-0576-4

Artemyev, A. V., Neishtadt, A. I., Vainchtein, D. L., et al. 2018, Communications in Nonlinear Science and Numerical Simulations, 65, 111, doi: 10.1016/j.cnsns.2018.05.004

Artemyev, A. V., Neishtadt, A. I., Vasiliev, A. A., & Mourenas, D. 2021, PhRvE, 104, 055203, doi: 10.1103/PhysRevE.104.055203

Artemyev, A. V., Shi, X., Liu, T. Z., et al. 2022, Journal of Geophysical Research (Space Physics), 127, e29820, doi: 10.1029/2021JA029820

Burch, J. L., Moore, T. E., Torbert, R. B., & Giles, B. L. 2016, SSRv, 199, 5, doi: 10.1007/s11214-015-0164-9

Chen, L., Thorne, R. M., Li, W., & Bortnik, J. 2013, J. Geophys. Res., 118, 1074, doi: 10.1029/2012JA018343

Chernikov, A. A., Schmidt, G., & Neishtadt, A. I. 1992, Physical Review Letters, 68, 1507, doi: 10.1103/PhysRevLett.68.1507

Chu, C., Zhang, H., Sibeck, D., et al. 2017, Annales Geophysicae, 35, 443, doi: 10.5194/angeo-35-443-2017

Collinson, G., Halekas, J., Grebowsky, J., et al. 2015, Geophys. Res. Lett., 42, 9121, doi: 10.1002/2015GL065079

Eastwood, J. P., Lucek, E. A., Mazelle, C., et al. 2005, SSRv, 118, 41, doi: 10.1007/s11214-005-3824-3

Frantsuzov, V. A., Artemyev, A. V., Shustov, P. I., & Zhang, X. J. 2022, Physics of Plasmas, 29, 052901, doi: 10.1063/5.0085953

Fu, X., Cowee, M. M., Friedel, R. H., et al. 2014, Journal of Geophysical Research (Space Physics), 119, 8288, doi: 10.1002/2014JA020364

Gary, S. P. 2005, Theory of Space Plasma Microinstabilities, Cambridge Atmospheric and Space (Cambridge University Press)

Gary, S. P., & Feldman, W. C. 1977, J. Geophys. Res., 82, 1087, doi: 10.1029/JA082i007p01087

Gosling, J. T., Thomsen, M. F., Bame, S. J., et al. 1982, Geophys. Res. Lett., 9, 1333, doi: 10.1029/GL009i012p01333

Gu, W., Chen, L., Xia, Z., & Horne, R. B. 2021, Geophys. Res. Lett., 48, e93987, doi: 10.1029/2021GL093987

Gurnett, D. A., & Bhattacharjee, A. 2005, Introduction to Plasma Physics

Hull, A. J., Muschietti, L., Oka, M., et al. 2012, J. Geophys. Res., 117, 12104, doi: 10.1029/2012JA017870

Inan, U. S., & Bell, T. F. 1977, J. Geophys. Res., 82, 2819, doi: 10.1029/JA082i019p02819

Karpman, V. I. 1974, SSRv, 16, 361, doi: 10.1007/BF00171564

Karpman, V. I., Istomin, J. N., & Shklyar, D. R. 1974, Plasma Physics, 16, 685, doi: 10.1088/0032-1028/16/8/001

Kennel, C. F. 1966, Physics of Fluids, 9, 2190, doi: 10.1063/1.1761588

—. 1969, Reviews of Geophysics and Space Physics, 7, 379, doi: 10.1029/RG007i001p00379

Kennel, C. F., & Engelmann, F. 1966, Physics of Fluids, 9, 2377, doi: 10.1063/1.1761629

Kuramitsu, Y., & Krasnoselskikh, V. 2005, Physical Review Letters, 94, 031102, doi: 10.1103/PhysRevLett.94.031102
Le Contel, O., Retinò, A., Breuillard, H., et al. 2016, Geophys. Res. Lett., 43, 5943, doi: 10.1002/2016GL068968
Le Queau, D., & Roux, A. 1987, SoPh, 111, 59, doi: 10.1007/BF00145441
Li, W., Mourenas, D., Artemyev, A. V., et al. 2016, Geophys. Res. Lett., 43, 8867, doi: 10.1002/2016GL070386
Lichko, E., & Egedal, J. 2020, Nature Communications, 11, 2942, doi: 10.1038/s41467-020-16660-4
Lin, Y. 1997, J. Geophys. Res., 102, 24265, doi: 10.1029/97JA01989
—. 2002, Planet. Space Sci., 50, 577, doi: 10.1016/S0032-0633(02)00037-5
Liu, T. Z., Angelopoulos, V., Hietala, H., & Wilson, Lynn B., I. 2017a, Journal of Geophysical Research (Space Physics), 122, 7197, doi: 10.1002/2017JA024043
Liu, T. Z., Angelopoulos, V., & Lu, S. 2019, Science Advances, 5, eaaw1368, doi: 10.1126/sciadv.aaw1368
Liu, T. Z., Lu, S., Angelopoulos, V., Hietala, H., & Wilson, L. B. 2017b, Journal of Geophysical Research (Space Physics), 122, 9248, doi: 10.1002/2017JA024480
Liu, T. Z., Turner, D. L., Angelopoulos, V., & Omidi, N. 2016, Journal of Geophysical Research, 121, 5489, doi: 10.1002/2016JA022461
Liu, Z., Turner, D. L., Angelopoulos, V., & Omidi, N. 2015, Geophys. Res. Lett., 42, 7860, doi: 10.1002/2015GL065842
Lu, X., Zhang, H., Liu, T., et al. 2022, Journal of Geophysical Research (Space Physics), 127, e29981, doi: 10.1029/2021JA029981
Lyons, L. R., Thorne, R. M., & Kennel, C. F. 1972, J. Geophys. Res., 77, 3455, doi: 10.1029/JA077i019p03455
Nunn, D. 1971, Journal of Plasma Physics, 6, 291, doi: 10.1017/S0022377800006061
Oka, M., Wilson, III, L. B., Phan, T. D., et al. 2017, ApJL, 842, L11, doi: 10.3847/2041-8213/aa7759
Oka, M., Otsuka, F., Matsukiyo, S., et al. 2019, ApJ, 886, 53, doi: 10.3847/1538-4357/ab4a81
Omidi, N., Eastwood, J. P., & Sibeck, D. G. 2010, Journal of Geophysical Research (Space Physics), 115, A06204, doi: 10.1029/2009JA014828
Omidi, N., Lee, S. H., & Sibeck, D. G. 2021, Journal of Geophysical Research (Space Physics), 126, e28924, doi: 10.1029/2020JA028924
Omidi, N., Lee, S. H., Sibeck, D. G., et al. 2020, Journal of Geophysical Research (Space Physics), 125, e28058, doi: 10.1029/2020JA028058
Omidi, N., & Sibeck, D. G. 2007, Journal of Geophysical Research (Space Physics), 112, A01203, doi: 10.1029/2006JA011663
Omura, Y., Katoh, Y., & Summers, D. 2008, J. Geophys. Res., 113, 4223, doi: 10.1029/2007JA012622
O'Neil, T. 1965, Physics of Fluids, 8, 2255, doi: 10.1063/1.1761193
Page, B., Vasko, I. Y., Artemyev, A. V., & Bale, S. D. 2021, ApJL, 919, L17, doi: 10.3847/2041-8213/ac2748
Paschmann, G., & Schwartz, S. J. 2000a, in ESA Special Publication, Vol. 449, Cluster-II Workshop Multiscale / Multipoint Plasma Measurements, ed. R. A. Harris, 99
Paschmann, G., & Schwartz, S. J. 2000b, in ESA Special Publication, Vol. 449, Cluster-II Workshop Multiscale / Multipoint Plasma Measurements, ed. R. A. Harris, 99
Pollock, C., Moore, T., Jacques, A., et al. 2016, SSRv, 199, 331, doi: 10.1007/s11214-016-0245-4
Russell, C. T., Anderson, B. J., Baumjohann, W., et al. 2016, SSRv, 199, 189, doi: 10.1007/s11214-014-0057-3
Sagdeev, R. Z., & Shafranov, V. D. 1961, Soviet Phys. JETP, 12, 130
Schwartz, S. J., Chaloner, C. P., Christiansen, P. J., et al. 1985, Nature, 318, 269, doi: 10.1038/318269a0
Schwartz, S. J., Avanov, L., Turner, D., et al. 2018, Geophys. Res. Lett., 45, 11,520, doi: 10.1029/2018GL080189
Shi, X., Liu, T. Z., Angelopoulos, V., & Zhang, X.-J. 2020, Journal of Geophysical Research (Space Physics), 125, e27758, doi: 10.1029/2019JA027758

Shklyar, D. R., Chum, J., & Jiřícek, F. 2004, Annales Geophysicae, 22, 3589, doi: 10.5194/angeo-22-3589-2004

Shklyar, D. R., & Matsumoto, H. 2009, Surveys in Geophysics, 30, 55, doi: 10.1007/s10712-009-9061-7

Solovev, V. V., & Shkliar, D. R. 1986, Sov. Phys. JETP, 63, 272

Sonnerup, B. U. Ö., & Cahill, Jr., L. J. 1968, J. Geophys. Res., 73, 1757, doi: 10.1029/JA073i005p01757

Sonnerup, B. U. Ö., & Scheible, M. 2000, ESA Special Publication, Vol. 449, ISSI Book on Analysis Methods for Multi-Spacecraft Data, ed. G.Paschmann and Patrick W. D.

Tong, Y., Vasko, I. Y., Artemyev, A. V., Bale, S. D., & Mozer, F. S. 2019a, ApJ, 878, 41, doi: 10.3847/1538-4357/ab1f05

Tong, Y., Vasko, I. Y., Pulupa, M., et al. 2019b, ApJL, 870, L6, doi: 10.3847/2041-8213/aaf734

Treumann, R. A. 2009, The Astronomy and Astrophysics Review, 17, 409, doi: 10.1007/s00159-009-0024-2

Turner, D. L., Omidi, N., Sibeck, D. G., & Angelopoulos, V. 2013, Journal of Geophysical Research (Space Physics), 118, 1552, doi: 10.1002/jgra.50198

Turner, D. L., Lee, J. H., Claudepierre, S. G., et al. 2017, Journal of Geophysical Research (Space Physics), 122, 11,201, doi: 10.1002/2017JA024474

Turner, D. L., Wilson, L. B., Liu, T. Z., et al. 2018, Nature, 561, 206, doi: 10.1038/s41586-018-0472-9

Turner, D. L., Liu, T. Z., Wilson, L. B., et al. 2020, Journal of Geophysical Research (Space Physics), 125, e27707, doi: 10.1029/2019JA027707

Ucer, D., & Shapiro, V. D. 2001, Physical Review Letters, 87, 075001, doi: 10.1103/PhysRevLett.87.075001

Vainchtein, D., Zhang, X. J., Artemyev, A. V., et al. 2018, Journal of Geophysical Research (Space Physics), 123, 8149, doi: 10.1029/2018JA025654

Vasko, I. Y., Kuzichev, I. V., Artemyev, A. V., et al. 2020, Physics of Plasmas, 27, 082902, doi: 10.1063/5.0003401

Veltri, P., & Zimbardo, G. 1993, J. Geophys. Res., 98, 13335, doi: 10.1029/93JA01144

Verkhoglyadova, O. P., Tsurutani, B. T., & Lakhina, G. S. 2010, Journal of Geophysical Research (Space Physics), 115, A00F19, doi: 10.1029/2009JA014809

—. 2013, Journal of Geophysical Research (Space Physics), 118, 7695, doi: 10.1002/2013JA019371

Verscharen, D., Chandran, B. D. G., Boella, E., et al. 2022, Frontiers in Astronomy and Space Sciences, 9, 951628, doi: 10.3389/fspas.2022.951628

Vu, A., Liu, T. Z., Zhang, H., & Delamere, P. 2022, Journal of Geophysical Research (Space Physics), 127, e29973, doi: 10.1029/2021JA029973

Wilson, L. B., Sibeck, D. G., Turner, D. L., et al. 2016, PhRvL, 117, 215101, doi: 10.1103/PhysRevLett.117.215101

Wilson, L. B., Koval, A., Sibeck, D. G., et al. 2013a, J. Geophys. Res., 118, 957, doi: 10.1029/2012JA018186

Wilson, L. B., Koval, A., Szabo, A., et al. 2013b, J. Geophys. Res., 118, 5, doi: 10.1029/2012JA018167

Zhang, H., Zong, Q., Connor, H., et al. 2022, SSRv, 218, 40, doi: 10.1007/s11214-021-00865-0

Zhang, X. J., Mourenas, D., Artemyev, A. V., et al. 2019, Geophys. Res. Lett., 46, 7182, doi: 10.1029/2019GL083833